Science Advances
AAAS

Supplementary Materials for

Flexible artificial Si-In-Zn-O/ion gel synapse and its application to sensory-neuromorphic system for sign language translation

Seyong Oh, Jeong-Ick Cho, Byeong Hyeon Lee, Seunghwan Seo, Ju-Hee Lee, Hyongsuk Choo, Keun Heo, Sang Yeol Lee*, Jin-Hong Park*

*Corresponding author. Email: sylee2020@gachon.ac.kr (S.Y.L.); jhpark9@skku.edu (J.-H.P.)

Published 29 October 2021, *Sci. Adv.* **7**, eabg9450 (2021)
DOI: 10.1126/sciadv.abg9450

This PDF file includes:

Figs. S1 to S13
Tables S1 and S2
References

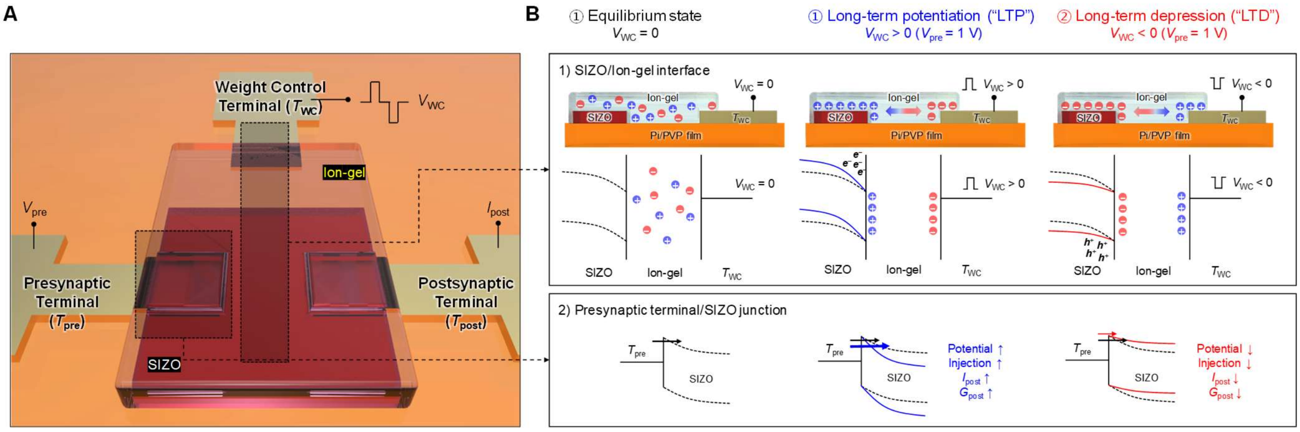

Fig. S1. Weight update mechanism of the SIZO/ion-gel synaptic device. (**A**) Device configuration of the flexible synaptic device based on a SIZO/ion-gel hybrid structure. (**B**) Illustrations and energy band diagrams of the ion movement in the SIZO/ion-gel interface (top panel) and energy band diagrams describing the surface potential in the presynaptic terminal/SIZO junction (bottom panel), according to the applied V_{WC}.

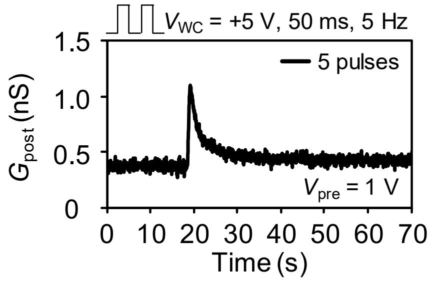

Fig. S2. Conductance response with respect to voltage pulses. On applying a voltage pulse with an amplitude of +5 V and duration of 50 ms, the conductance momentarily increased from 0.36 to 1.43 nS, and subsequently, it slowly decreased to 0.44 nS. As described in the main article, when a voltage pulse is applied, the ions accumulate near the interface and are also adsorbed into the existing defects in the SIZO channel region. The ions that from the EDL rapidly diffuse into the ion-gel; however, the adsorbed ions are expected to be removed slowly, which likely causes the short-term and long-term synaptic plasticity.

A

B

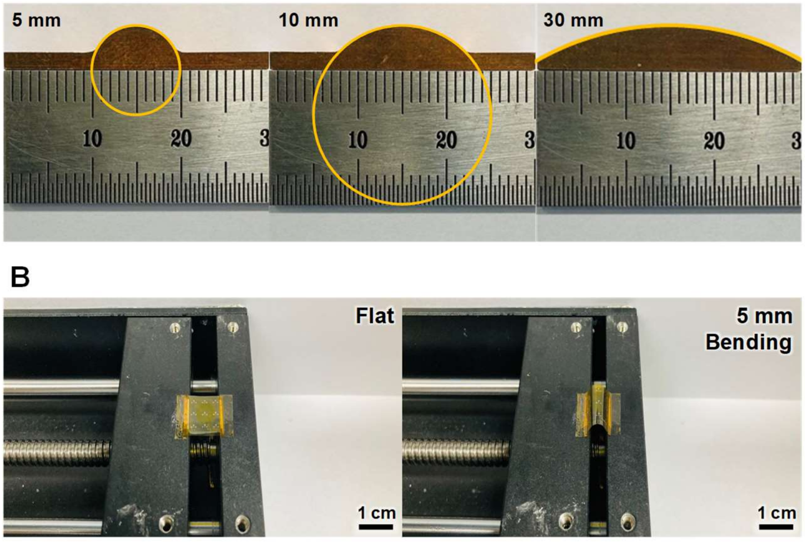

Fig. S3. Optical images of the test equipment for mechanical flexibility and durability. (**A**) Arch-shaped metal bars with a radius of 5 mm, 10 mm, and 30 mm. (**B**) Step motor controller (SMC-100, ECOPIA) before bending (left panel) and after 5 mm bending (right panel) (Photo Credit: Jeong-Ick Cho, Sungkyunkwan University).

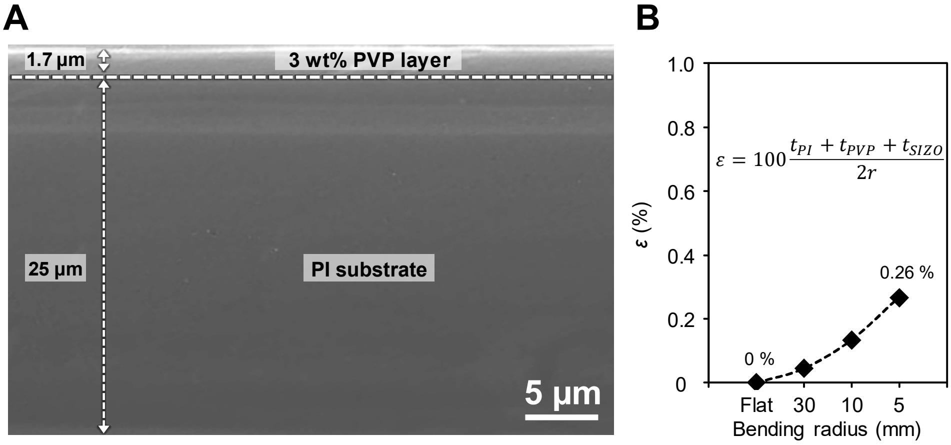

Fig. S4. Bending strain investigation. (**A**) Cross-sectional SEM image of the 3 wt% PVP-coated PI substrate. (**B**) Calculated bending strain (ε) with respect to the bending radius from 30 to 5 mm of the SIZO/ion-gel flexible synaptic device. The ε value can be estimated using the equation inserted in Fig.S4B. Here, t_{PI} = 25 µm, $t_{\mathrm{PVP}} \approx$ 1.7 µm, and t_{SIZO} = 30 nm, which denotes the thickness of the PI substrate, PVP layer, and SIZO channel layer, respectively, and r is the bending radius.

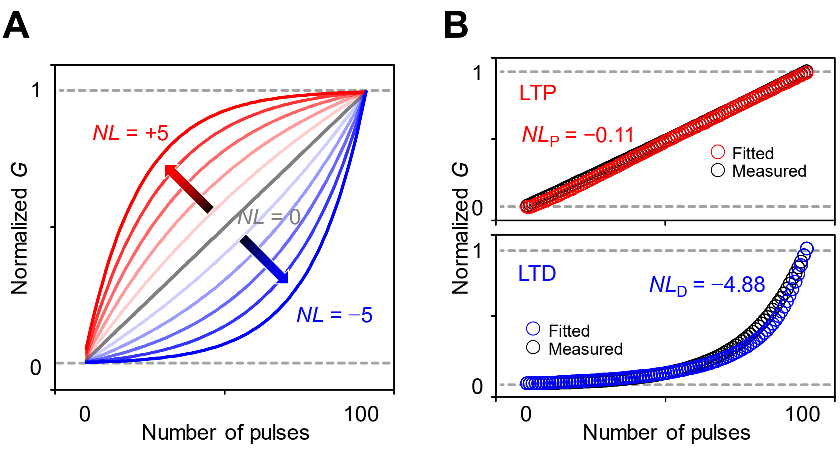

Fig. S5. Nonlinearity extraction method of the LTP/D characteristic curves. (**A**) Normalized G_{LTP} and G_{LTD} curves (i.e. the normalized LTP/D characteristic curves) with respect to *NL* ranging from 0 to ±5. (**B**) Measured/fitted curves in LTP (upper panel) and LTD (lower panel) regions, where $NL_{L/D}$ = −0.11/−4.88.

There are several methods to evaluate the *NL* of the LTP/LTD characteristic curve (*57*−*60*). Among them, we chose a method to tune A_P and A_D for finding the G_{LTP} and G_{LTD} curves best matched to the measured LTP/LTD curves (*5*, *6*). The conductance curve model with the number of pulses (*P*) is represented as the following equations:

$$G_{LTP} = B_P \cdot (1 - \exp(-P/A_P)) + G_{min}, \tag{1}$$

$$G_{LTD} = -B_D \cdot (1 - \exp((P - P_{max})/A_D)) + G_{max}, \tag{2}$$

$$B_{P,D} = (G_{max} - G_{min})/(1 - \exp(-P_{max}/A_{P,D})) \tag{3}$$

where G_{LTP} and G_{LTD} are the conductance values for LTP and LTD, respectively. G_{max}, G_{min}, and P_{max} are the measured data that represent the maximum conductance, minimum conductance, and maximum pulse number, respectively. $B_{P,D}$ is a fitting constant to normalize the conductance range for the LTP and LTD regions. A_P and A_D are parameters that determine the nonlinearities of the weight update in the LTP and LTD regions, which are directly related to the *NL* values.

The G_{LTP} and G_{LTD} curves with respect to the *NL* ranging from 0 to ±5 are displayed in Fig. S5A. By adjusting the A_P and A_D values, the G_{LTP} and G_{LTD} curves are fitted to the measured LTP/LTD curves, and accordingly the *NL* values are determined (Fig. S5B).

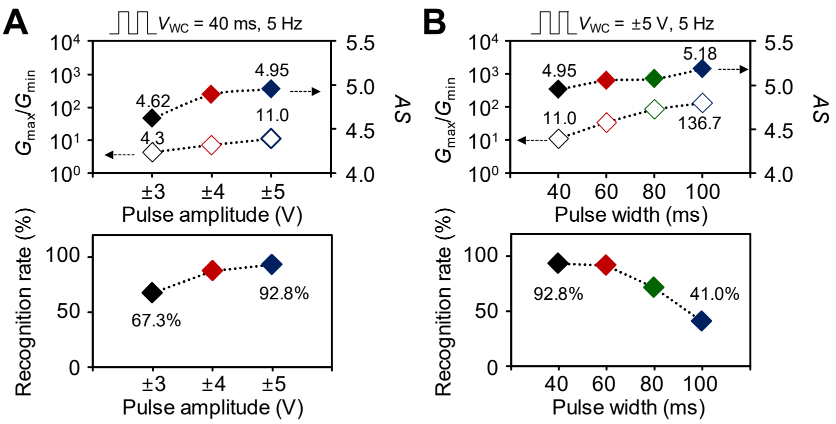

Fig. S6. Investigation of the learning accuracy with respect to the pulse conditions. (**A**) Extracted G_{max}/G_{min} and *AS* values with respect to the pulse amplitude from ±3 to ±5 V (top panel) and estimated recognition rates (bottom panel). (**B**) Extracted G_{max}/G_{min} and *AS* values with respect to the pulse width from 40 to 100 ms (top panel) and estimated recognition rates (bottom panel).

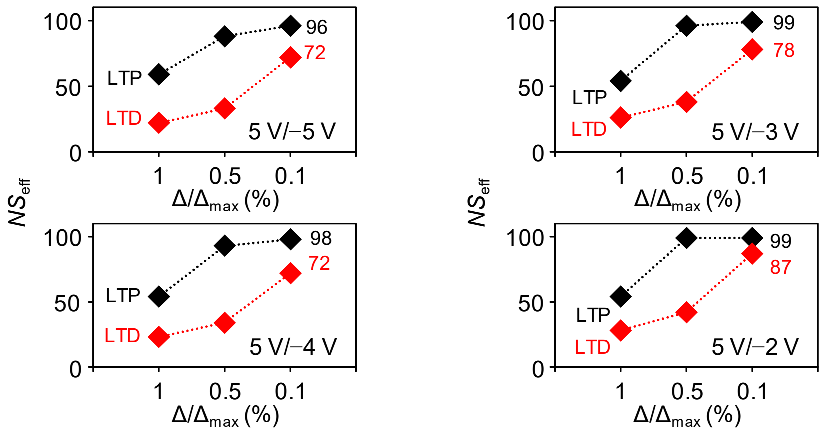

Fig. S7. Effective number of conductance states (*NS*$_{eff}$) according to the ratio between Δ*G* and *G*$_{max}$−*G*$_{min}$ (Δ/Δ$_{max}$). *NS*$_{eff}$ vs. Δ/Δ$_{max}$ with respect to the depressing pulse amplitude ranging from −5 V to −2 V.

From the LTP/D characteristics in Fig. 3D, we extracted the *NS*$_{eff}$ values when Δ/Δ$_{max}$ was greater than 1 %, 0.5 %, and 0.1 % (Fig. S7). For all depressing pulse-amplitude cases, the *NS*$_{eff}$ value increased significantly as the Δ/Δ$_{max}$ decreased from 1 to 0.1 %. Especially, in the 5 V/−2 V-case, the *NS*$_{eff}$ in the LTP and LTD regions reached 99 and 87, respectively, even under the strict condition: Δ/Δ $_{max}$ > 0.1%. This means that 99 % and 87 % of the total conductance states were effectively usable, indicating that our synaptic device possessed an enough number of conductance states between *G*$_{max}$ and *G*$_{min}$.

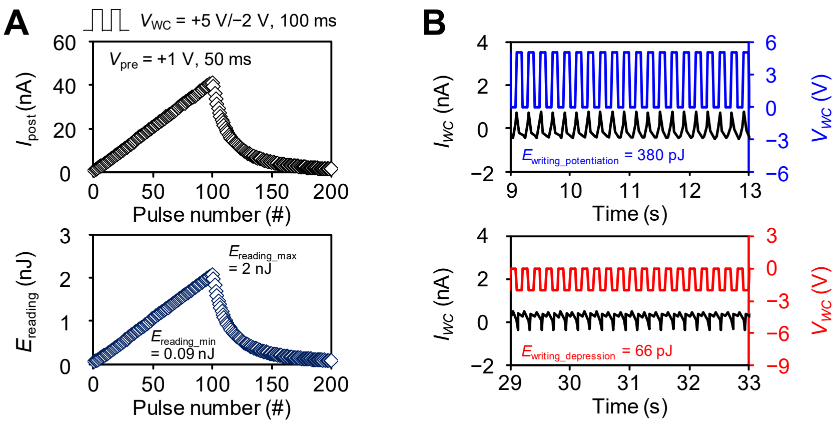

Fig. S8. Energy consumption of the SIZO/ion-gel synaptic device. (**A**) Measured I_{post} (upper panel) and calculated $E_{reading}$ (bottom panel) with respect to the V_{WC} pulse number. (**B**) Measured I_{WC} and calculated $E_{writing}$ with respect to the potentiation (top panel) and depression pulses (bottom panel).

We roughly calculated the reading ($E_{reading}$) and writing energy ($E_{writing}$) using the equations below:

$$E_{reading} = V_{pre} \times I_{post} \times t_{pre} \quad (4)$$

$$E_{writing} = V_{WC} \times I_{WC} \times t_{WC} \,, \quad (5)$$

where V_{pre}, I_{post}, and t_{read} represent the magnitude of V_{pre}, the peak value of I_{post}, and the pulse duration of V_{pre}, respectively. V_{WC}, I_{WC}, and t_{WC} denote the magnitude of V_{WC}, the peak value of I_{WC}, and the pulse duration of V_{WC}, respectively (*39*, *41*).

As shown in Fig. S8, $E_{reading}$ was approximately distributed from 0.09 to 2.0 nJ. The value of $E_{writing}$ for the potentiation pulse was +5 V × 0.76 nA × 100 ms = 380 pJ and that for the depression pulse was −2 V × −0.33 nA × 100 ms = 66 pJ. These values are slightly higher than the energies reported in recent works (below 10 pJ) (*61*–*63*).

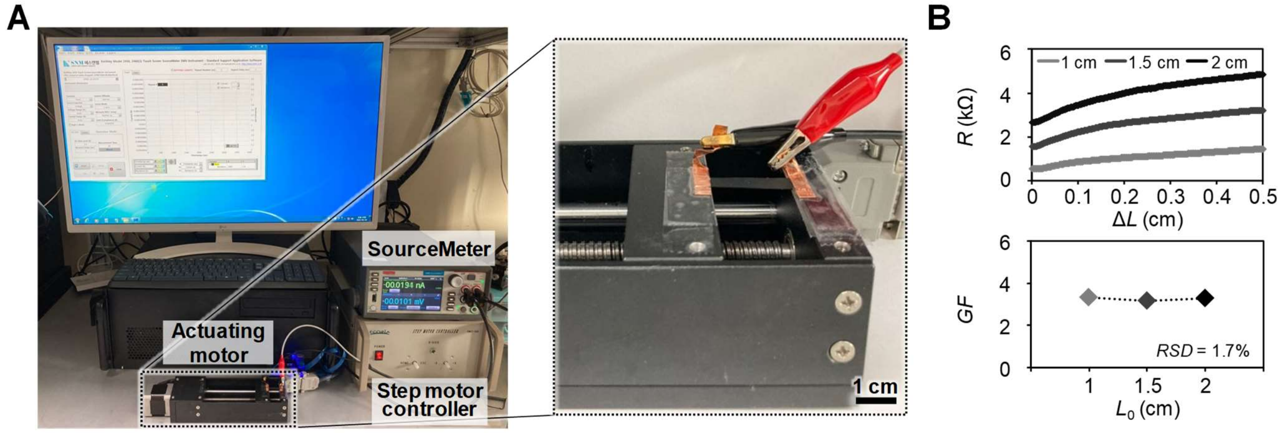

Fig. S9. The stretching test platform for the electrical measurement CNT/SEBS stretchable sensor. (**A**) Measurement setup consisting of an actuating motor, a step motor controller, and a SourceMeter. (**B**) Resistance (*R*) according to the length change (ΔL) of the stretchable resistive sensor with the initial length (L_0) of 1 cm, 1.5 cm, and 2 cm, where the stretchable sensor was gradually extended to 0.5 cm (the top panel). Strain Gauge Factor (*GF*) with respect to L_0 of the sensor (the bottom panel) (Photo Credit: Jeong-Ick Cho, Sungkyunkwan University).

As shown in Fig. S9A, to investigate the mechanical deformation with respect to the resistance of stretchable sensors, a stretching test platform was employed, which consists of an actuating motor (Jaeil optical system), a step motor controller (SMC-100, ECOPIA), and a Keithley 2450 SourceMeter. The CNT/SEBS sensors were cut into three lengths of 1 cm, 1.5 cm, and 2 cm (the width was fixed at 0.5 cm), and the side parts of these sensors were attached to the test platform. The sensors were pulled gradually, and the change in *R* was monitored with a source-meter connected to both ends of the sensor.

The *R* values for 1 cm, 1.5 cm, and 2 cm were changed from 0.54 to 1.45, from 1.56 to 3.21, and from 2.66 to 4.85 kΩ as ΔL increased from 0 to 0.5 cm, respectively (the top panel of Fig. S9B). Then, *GF* was calculated as the following equation:

$$GF = \frac{\Delta R/R_0}{\Delta L/L_0}$$

where the ΔR is the difference between R_0 and *R* values. As shown in the bottom panel of Fig. S9B, the *GF* value with regard to L_0 of 1 cm, 1.5 cm, and 2 cm was 3.30, 3.18, and 3.29, respectively, and the *RSD* was only 1.7 %, indicating that the stretchable sensor had high reliability regardless of L_0.

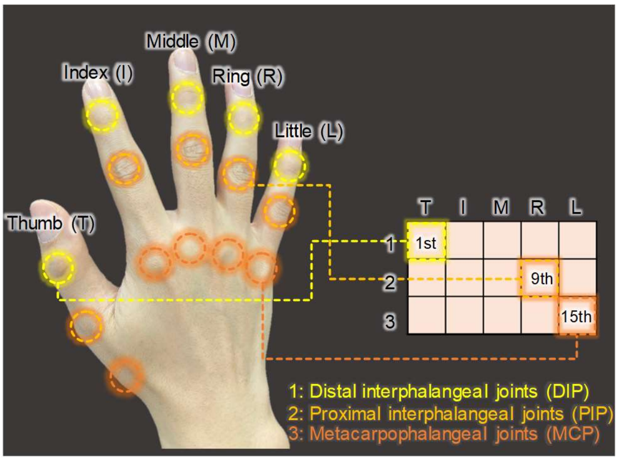

Fig. S10. Arrangement of the hand sign pattern with a size of 3 × 5 corresponding to each finger joint (Photo Credit: Jeong-Ick Cho, Sungkyunkwan University)**.**

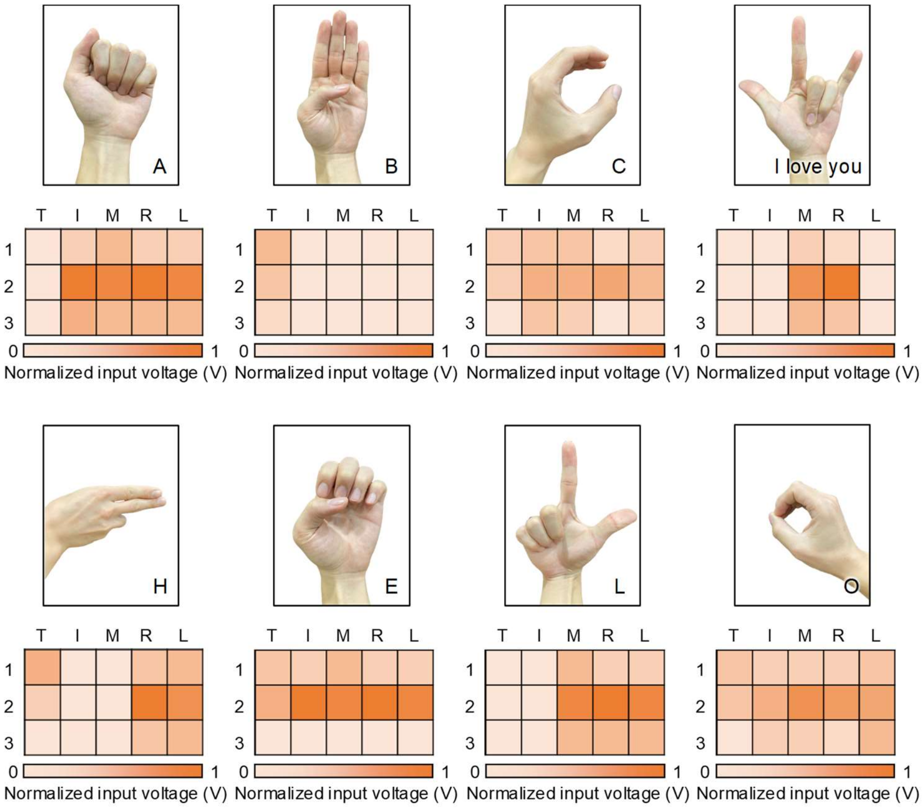

Fig. S11. Prepared hand sign patterns for "A", "B", "C", "I love you", "H", "E", "L", and "O".

To prepare the hand sign pattern data, we conducted the sensing and patterning process. First, the ΔR values for the 15 finger joints were measured using a 2-cm length stretchable sensor after gesturing a hand sign corresponding to "A", "B", "C", "I love you", "H", "E", "L", and "O" (see Fig. S9). Then, the measured ΔR of each finger joint was arranged onto a hand sign pattern with a size of 3 × 5 as shown in Fig. S10. Finally, all ΔR values in the pattern data were converted into a voltage form ranging from 0 to 1 V (Fig. S11) (Photo Credit: Jeong-Ick Cho, Sungkyunkwan University).

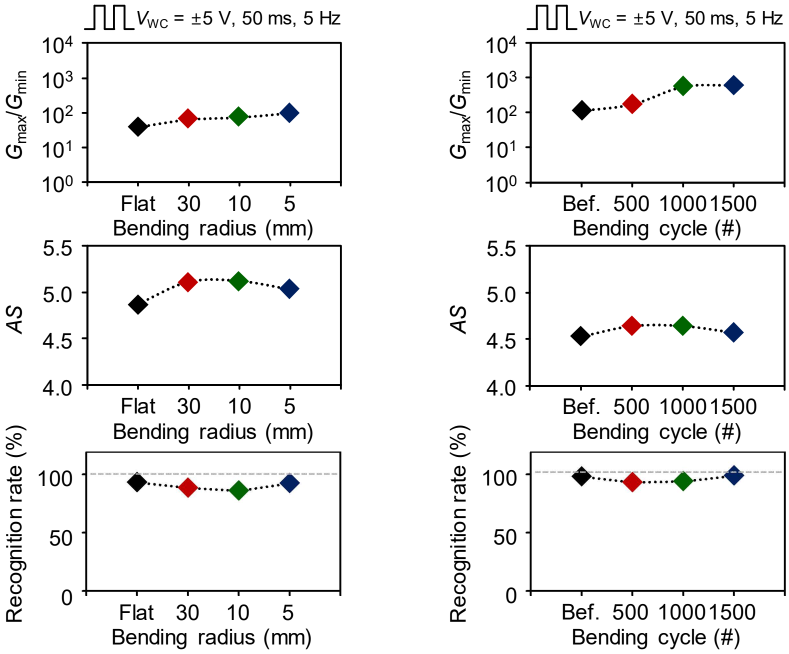

Fig. S12. G_{max}/G_{min} (top panel), *AS* (middle panel) values, and Recognition rates (bottom panel) with respect to bending radius (left panel) and bending cycles (right panel).

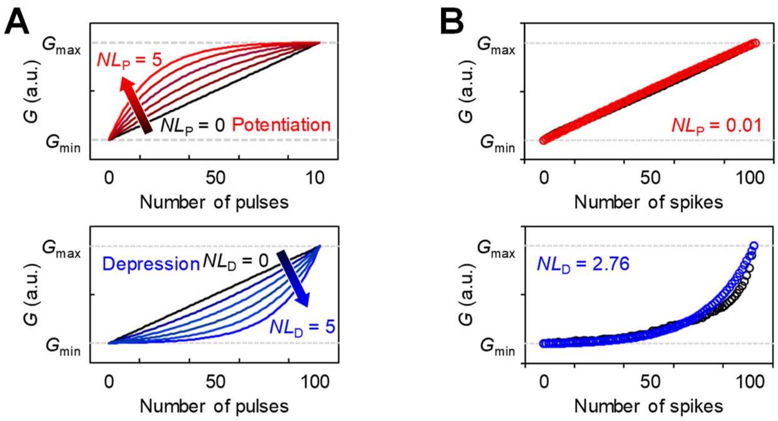

Fig. S13. Nonlinearity analysis of LTP/LTD curves for pattern recognition tasks. (**A**) LTP and LTD curves with respect to nonlinearity (*NL*) ranging from 0 to 5. (**B**) LTP and LTD curve fitting; $NL_P = 0.01$ and $NL_D = 2.76$.

As shown in Fig. S13, nonlinearity (*NL*) was obtained by fitting the LTP/LTD curves with the following weight update formula:

$$G_{n+1} = G_n + \Delta G_P = G_n + \alpha_P e^{-\beta_P \frac{G_n - G_{min}}{G_{max} - G_{min}}},$$

$$G_{n+1} = G_n + \Delta G_D = G_n - \alpha_D e^{-\beta_D \frac{G_{max} - G_n}{G_{max} - G_{min}}}.$$

Here, G_{n+1} and G_n represent the conductance values of the synaptic device when the n+1th and nth spikes are applied, respectively. G_{max} and G_{min} represent the maximum and minimum conductance values, respectively. The parameters α and *NL* indicate the step size of the conductance and the nonlinearity, respectively. As shown in Fig. S13, a larger *NL* corresponds to higher nonlinearity. The nonlinearity values obtained from the fitted LTP/LTD curves were 0.01/2.76. As depicted in Fig. S13B, the fitted theoretical LTP/LTD curves are highly similar to the experimentally obtained curves.

Channel	IZO	ITO	IWO	IGZO	IGZO	SnO_2	This work
							SIZO
Dielectric	PSG	Chitosan	Chitosan	Al_2O_3	PZT	$LiClO_4$	**Ion-gel**
Substrate	Si membrane	PET	PET	PET	Mica	PEN	**PI film**
Bending radius	10 mm	20 mm	30 mm	9.5 mm	4 mm	8 mm	**5 mm**
Bending cycle	2.0×10^2	1.0×10^3	1.0×10^3	1.0×10^1	4.0×10^2	1.0×10^1	$\mathbf{1.5\times10^3}$
Reference	(*64*)	(*65*)	(*66*)	(*67*)	(*68*)	(*69*)	**-**

Table S1. Performance benchmark with regard to the mechanical flexibility (bending radius) and durability (bending cycle) in comparison with other AOS-based flexible synapses.

	Ag:a-Si	TaO_x/HfO_x	PCMO	AlO_x/HfO_2	GST PCM	Epi-RAM	HZO FeFET	This work	Ideal
								SIZO/ion-gel	
Nonlinearity (P/D)	2.4/−4.88	0.04/−0.63	3.68/−6.76	1.94/−0.61	0.105/2.4	0.5/−0.5	1.75/1.46	**0.1/−2.4**	0/0
ON/OFF ratio	12.5	10	6.84	4.43	19.8	50.2	45	**23.0**	>10
# of conductance states	97	128	50	40	100–120	64	32	**100**	>64
Cycle-to-cycle variation	3.5%	3.7%	<1%	5%	1.5%	2%	<0.5%	**<1%**	0%
Online learning accuracy	~72%	~80%	~33%	~20%	89%	92%	88%	**88.5%**	93.5%
Reference	(*70*)	(*71*)	(*72*)	(*73*)	(*74*)	(*75*)	(*76*)	**-**	-

Table S2. Comparison of the proposed synaptic device and other synaptic devices in terms of the learning accuracy predicted using NeuroSim+ MNIST simulator (*56*)

REFERENCES AND NOTES

1. Y. Lee, J. Park, A. Choe, S. Cho, J. Kim, H. Ko, Mimicking human and biological skins for multifunctional skin electronics. *Adv. Funct. Mater.* **30**, 1904523 (2020).

2. Y. Song, J. Min, Y. Yu, H. Wang, Y. Yang, H. Zhang, W. Gao, Wireless battery-free wearable sweat sensor powered by human motion. *Sci. Adv.* **6**, 10.1126/sciadv.aay9842 (2020).

3. Z. Zhang, T. He, M. Zhu, Z. Sun, Q. Shi, J. Zhu, B. Dong, M. R. Yuce, C. Lee, Deep learning-enabled triboelectric smart socks for IoT-based gait analysis and VR applications. *npj Flex. Electron.* **4**, 29 (2020).

4. J. Kim, A. S. Campbell, B. E. F. de Ávila, J. Wang, Wearable biosensors for healthcare monitoring. *Nat. Biotechnol.* **37**, 389–406 (2019).

5. S. Lee, S. Gandla, M. Naqi, U. Jung, H. Youn, D. Pyun, Y. Rhee, S. Kang, H. J. Kwon, H. Kim, M. G. Lee, S. Kim, All-day mobile healthcare monitoring system based on heterogeneous stretchable sensors for medical emergency. *IEEE Trans. Ind. Electron.* **67**, 8808–8816 (2020).

6. S. Gandla, M. Naqi, M. Lee, J. J. Lee, Y. Won, P. Pujar, J. Kim, S. Lee, S. Kim, Highly linear and stable flexible temperature sensors based on laser-induced carbonization of polyimide substrates for personal mobile monitoring. *Adv. Mater. Technol.* **5**, 2000014 (2020).

7. H. Joo, Y. Lee, J. Kim, J. S. Yoo, S. Yoo, S. Kim, A. K. Arya, S. Kim, S. H. Choi, N. Lu, H. S. Lee, S. Kim, S. T. Lee, D. H. Kim, Soft implantable drug delivery device integrated wirelessly with wearable devices to treat fatal seizures. *Sci. Adv.* **7**, 10.1126/sciadv.abd4639 (2021).

8. W. Xu, S.-Y. Min, H. Hwang, T.-W. Lee, Organic core-sheath nanowire artificial synapses with femtojoule energy consumption. *Sci. Adv.* **2**, e1501326 (2016).

9. Y. Fu, L. A. Kong, Y. Chen, J. Wang, C. Qian, Y. Yuan, J. Sun, Y. Gao, Q. Wan, Flexible neuromorphic architectures based on self-supported multiterminal organic transistors. *ACS Appl. Mater. Interfaces* **10**, 26443–26450 (2018).

10. J. W. Borchert, U. Zschieschang, F. Letzkus, M. Giorgio, R. T. Weitz, M. Caironi, J. N. Burghartz, S. Ludwigs, H. Klauk, Flexible low-voltage high-frequency organic thin-film transistors. *Sci. Adv.* **6**, 10.1126/sciadv.aaz5156 (2020).

11. L. Gao, Flexible device applications of 2D semiconductors. *Small* **13**, 1603994 (2017).

12. H. Park, D. S. Oh, K. J. Lee, D. Y. Jung, S. Lee, S. Yoo, S. Y. Choi, Flexible and transparent thin-film transistors based on two-dimensional materials for active-matrix display. *ACS Appl. Mater. Interfaces* **12**, 4749–4754 (2020).

13. H. Tan, Q. Tao, I. Pande, S. Majumdar, F. Liu, Y. Zhou, P. O. Å. Persson, J. Rosen, S. van Dijken, Tactile sensory coding and learning with bio-inspired optoelectronic spiking afferent nerves. *Nat. Commun.* **11**, 1369 (2020).

14. K. T. Kim, S. H. Kang, J. Kim, J. S. Heo, Y. H. Kim, S. K. Park, An ultra-flexible solution-processed metal-oxide/carbon nanotube complementary circuit amplifier with highly reliable electrical and mechanical stability. *Adv. Electron. Mater.* **6**, 1900845 (2020).

15. J. Kim, S. Kwon, Y. K. Kang, Y. Kim, M. Lee, K. Han, A. Facchetti, M. Kim, S. K. Park, A skin-like two-dimensionally pixelized full-color quantum dot photodetector. *Sci. Adv.* **5**, 10.1126/sciadv.aax8801 (2019).

16. B. Wang, A. Thukral, Z. Xie, L. Liu, X. Zhang, W. Huang, X. Yu, C. Yu, T. J. Marks, A. Facchetti, Flexible and stretchable metal oxide nanofiber networks for multimodal and monolithically integrated wearable electronics. *Nat. Commun.* **11**, 10.1126/sciadv.aax8801 (2020).

17. K. Nomura, H. Ohta, A. Takagi, T. Kamiya, M. Hirano, H. Hosono, Room-temperature fabrication of transparent flexible thin-film transistors using amorphous oxide semiconductors. *Nature* **432**, 488- 492 (2004).

18. P. Grey, D. Gaspar, I. Cunha, R. Barras, J. T. Carvalho, J. R. Ribas, E. Fortunato, R. Martins, L. Pereira, Handwritten oxide electronics on paper. *Adv. Mater. Technol.* **2**, 2–8 (2017).

19. J. Y. Choi, S. Kim, B.-U. Hwang, N.-E. Lee, S. Y. Lee, Flexible SiInZnO thin film transistor with organic/inorganic hybrid gate dielectric processed at 150°C. *Semicond. Sci. Technol.* **31**, 12507 (2016).

20. K. Sim, Z. Rao, Z. Zou, F. Ershad, J. Lei, A. Thukral, J. Chen, Q. A. Huang, J. Xiao, C. Yu, Metal oxide semiconductor nanomembrane–based soft unnoticeable multifunctional electronics for wearable human-machine interfaces. *Sci. Adv.* **5**, 1–11 (2019).

21. M. Zulqarnain, S. Stanzione, G. Rathinavel, S. Smout, M. Willegems, K. Myny, E. Cantatore, A flexible ECG patch compatible with NFC RF communication. *npj Flex. Electron.* **4**, 13 (2020).

22. K. Yang, S. Yuan, Y. Huan, J. Wang, L. Tu, J. Xu, Z. Zou, Y. Zhan, L. Zheng, F. Seoane, Tunable flexible artificial synapses: A new path toward a wearable electronic system. *npj Flex. Electron.* **2**, 20 (2018).

23. Y. Lee, J. Y. Oh, W. Xu, O. Kim, T. R. Kim, J. Kang, Y. Kim, D. Son, J. B. H. Tok, M. J. Park, Z. Bao, T. W. Lee, Stretchable organic optoelectronic sensorimotor synapse. *Sci. Adv.* **4**, 10.1126/sciadv.aat7387 (2018).

24. D. Choi, M. K. Song, T. Sung, S. Jang, J. Y. Kwon, Energy scavenging artificial nervous system for detecting rotational movement. *Nano Energy* **74**, 104912 (2020).

25. Y. R. Lee, T. Q. Trung, B. U. Hwang, N. E. Lee, A flexible artificial intrinsic-synaptic tactile sensory organ. *Nat. Commun.* **11**, 2753 (2020).

26. H. Shim, K. Sim, F. Ershad, P. Yang, A. Thukral, Z. Rao, H. J. Kim, Y. Liu, X. Wang, G. Gu, L. Gao, X. Wang, Y. Chai, C. Yu, Stretchable elastic synaptic transistors for neurologically integrated soft engineering systems. *Sci. Adv.* **5**, 10.1126/sciadv.aax4961 (2019).

27. S. Ham, M. Kang, S. Jang, J. Jang, S. Choi, T. W. Kim, G. Wang, One-dimensional organic artificial multi-synapses enabling electronic textile neural network for wearable neuromorphic applications. *Sci. Adv.* **6**, 10.1126/sciadv.aba1178 (2020).

28. Y. Y. Zhao, W. J. Sun, J. Wang, J. H. He, H. Li, Q. F. Xu, N. J. Li, D. Y. Chen, J. M. Lu, All-inorganic ionic polymer-based memristor for high-performance and flexible artificial synapse. *Adv. Funct. Mater.* **30**, 1–8 (2020).

29. D. W. Kim, J. C. Yang, S. Lee, S. Park, Neuromorphic processing of pressure signal using integrated sensor-synaptic device capable of selective and reversible short- and long-term plasticity operation. *ACS Appl. Mater. Interfaces* **12**, 23207–23216 (2020).

30. C. Wan, P. Cai, X. Guo, M. Wang, N. Matsuhisa, L. Yang, Z. Lv, Y. Luo, X. J. Loh, X. Chen, An artificial sensory neuron with visual-haptic fusion. *Nat. Commun.* **11**, 4602 (2020).

31. Y. Zang, H. Shen, D. Huang, C. A. Di, D. Zhu, A dual-organic-transistor-based tactile-perception system with signal-processing functionality. *Adv. Mater.* **29**, 1606088 (2017).

32. Y. Kim, A. Chortos, W. Xu, Y. Liu, J. Y. Oh, D. Son, J. Kang, A. M. Foudeh, C. Zhu, Y. Lee, S. Niu, J. Liu, R. Pfattner, Z. Bao, T. W. Lee, A bioinspired flexible organic artificial afferent nerve. *Science* **360**, 998–1003 (2018).

33. S. Kim, Y. Lee, H.-D. Kim, S.-J. Choi, A tactile sensor system with sensory neurons and a perceptual synaptic network based on semivolatile carbon nanotube transistors. *NPG Asia Mater.* **12**, 76 (2020).

34. W. G. Regehr, L. F. Abbott, Synaptic computation. *Nature* **431**, 796–803 (2004).

35. A. Richter, J. J. BelBruno, Characterization of functional states in nicotine- and cotinine-imprinted poly(4-vinylphenol) films by nanoindentation. *J. Appl. Polym. Sci.* **124**, 2798–2806 (2012).

36. S. Kim, M. Lim, Y. Kim, H. D. Kim, S. J. Choi, Impact of synaptic device variations on pattern recognition accuracy in a hardware neural network. *Sci. Rep.* **8**, 2638 (2018).

37. J. Sun, S. Oh, Y. Choi, S. Seo, M. J. Oh, M. Lee, W. B. Lee, P. J. Yoo, J. H. Cho, J. H. Park, Optoelectronic synapse based on IGZO-alkylated graphene oxide hybrid structure. *Adv. Funct. Mater.* **28**, 1804397 (2018).

38. S. Seo, J.-J. Lee, H.-J. Lee, H. W. Lee, S. Oh, J. J. Lee, K. Heo, J.-H. Park, Recent progress in artificial synapses based on two-dimensional van der waals materials for brain-inspired computing. *ACS Appl. Electron. Mater.* **2**, 371–388 (2020).

39. S. Seo, B. S. Kang, J. J. Lee, H. J. Ryu, S. Kim, H. Kim, S. Oh, J. Shim, K. Heo, S. Oh, J. H. Park, Artificial van der waals hybrid synapse and its application to acoustic pattern recognition. *Nat. Commun.* **11**, 3936 (2020).

40. S. Oh, S. Jung, M. H. Ali, J. H. Kim, H. Kim, J. H. Park, Highly stable artificial synapse consisting of low-surface defect van der waals and self-assembled materials. *ACS Appl. Mater. Interfaces* **12**, 38299–38305 (2020).

41. Y. Choi, S. Oh, C. Qian, J. H. Park, J. H. Cho, Vertical organic synapse expandable to 3D crossbar array. *Nat. Commun.* **11**, 4595 (2020).

42. J. Huang, J. Chen, R. Yu, Y. Zhou, Q. Yang, E. Li, Q. Chen, H. Chen, T. Guo, Tuning the synaptic behaviors of biocompatible synaptic transistor through ion-doping. *Org. Electron.* **89**, 106019 (2021).

43. T. S. Kim, Y. Lee, W. Xu, Y. H. Kim, M. Kim, S. Y. Min, T. H. Kim, H. W. Jang, T. W. Lee, Direct-printed nanoscale metal-oxide-wire electronics. *Nano Energy* **58**, 437–446 (2019).

44. H. L. Park, Y. Lee, N. Kim, D. G. Seo, G. T. Go, T. W. Lee, Flexible neuromorphic electronics for computing, soft robotics, and neuroprosthetics. *Adv. Mater.* **32**, 1903558 (2020).

45. S. Yang, J. Y. Bak, S. M. Yoon, M. K. Ryu, H. Oh, C. S. Hwang, G. H. Kim, S. H. K. Park, J. Jang, Low-temperature processed flexible In-Ga-Zn-O thin-film transistors exhibiting high electrical performance. *IEEE Electron Device Lett.* **32**, 1692–1694 (2011).

46. B. J. Kim, H. Jang, S. K. Lee, B. H. Hong, J. H. Ahn, J. H. Cho, High-performance flexible graphene field effect transistors with ion gel gate dielectrics. *Nano Lett.* **10**, 3464–3466 (2010).

47. J. Pu, Y. Yomogida, K. Liu, L. Li, Y. Iwasa, T. Takenobu, Highly flexible MoS_2 thin-film transistors with ion gel dielectrics. *Nano Lett.* **13**, 10–14 (2012).

48. S. Yu, Neuro-inspired computing with emerging nonvolatile memorys. *Proc. IEEE* **106**, 260–285 (2018).

49. Z. Zhou, K. Chen, X. Li, S. Zhang, Y. Wu, Y. Zhou, K. Meng, C. Sun, Q. He, W. Fan, E. Fan, Z. Lin, X. Tan, W. Deng, J. Yang, J. Chen, Sign-to-speech translation using machine-learning-assisted stretchable sensor arrays. *Nat. Electron.* **3**, 571–578 (2020).

50. F. Zhou, Y. Chai, Near-sensor and in-sensor computing. *Nat. Electron.* **3**, 664–671 (2020).

51. Y. Wu, Y. Liu, Y. Zhou, Q. Man, C. Hu, W. Asghar, F. Li, Z. Yu, J. Shang, G. Liu, M. Liao, R. W. Li, A skin-inspired tactile sensor for smart prosthetics. *Sci. Robot.* **3**, 10.1126/scirobotics.aat0429 (2018).

52. C. Zhang, W. Bin Ye, K. Zhou, H. Y. Chen, J. Q. Yang, G. Ding, X. Chen, Y. Zhou, L. Zhou, F. Li, S. T. Han, Bioinspired artificial sensory nerve based on nafion memristor. *Adv. Funct. Mater.* **29**, 1808783 (2019).

53. Y. Liu, W. Yang, Y. Yan, X. Wu, X. Wang, Y. Zhou, Y. Hu, H. Chen, T. Guo, Self-powered high-sensitivity sensory memory actuated by triboelectric sensory receptor for real-time neuromorphic computing. *Nano Energy* **75**, 104930 (2020).

54. L. Wang, Y. Liu, Q. Liu, Y. Zhu, H. Wang, Z. Xie, X. Yu, Y. Zi, A metal-electrode-free, fully integrated, soft triboelectric sensor array for self-powered tactile sensing. *Microsyst. Nanoeng.* **6**, 59 (2020).

55. C. Qian, S. Oh, Y. Choi, S. Seo, J. Sun, J. H. Park, J. H. Cho, Rational band engineering of an organic double heterojunction for artificial synaptic devices with enhanced state retention and linear update of synaptic weight. *ACS Appl. Mater. Interfaces* **12**, 10737–10745 (2020).

56. Y. Luo, X. Peng, S. Yu, MLP+NeuroSimV3.0: Improving on-chip learning performance with device to algorithm optimizations, in *Proceedings of the International Conference on Neuromorphic Systems (ICONS'19)*, ACM, Knoxvillw, Tennessee, USA, 2019.

57. C. Sen Yang, D. S. Shang, N. Liu, E. J. Fuller, S. Agrawal, A. A. Talin, Y. Q. Li, B. G. Shen, Y. Sun, All-solid-state synaptic transistor with ultralow conductance for neuromorphic computing. *Adv. Funct. Mater.* **28**, 1804170 (2018).

58. L. Yin, C. Han, Q. Zhang, Z. Ni, S. Zhao, K. Wang, D. Li, M. Xu, H. Wu, X. Pi, D. Yang, Synaptic silicon-nanocrystal phototransistors for neuromorphic computing. *Nano Energy* **63**, 103859 (2019).

59. P. Y. Chen, X. Peng, S. Yu, Neurosim+: An integrated device-to-algorithm framework for benchmarking synaptic devices and array architectures, in *Proceedings of the 2017 IEEE International Electron Devices Meeting (IEDM)*, 2017.

60. C. Qian, S. Oh, Y. Choi, J. H. Kim, J. Sun, H. Huang, J. Yang, Y. Gao, J. H. Park, J. H. Cho, Solar-stimulated optoelectronic synapse based on organic heterojunction with linearly potentiated synaptic weight for neuromorphic computing. *Nano Energy* **66**, 104095 (2019).

61. J. Y. Gerasimov, R. Gabrielsson, R. Forchheimer, E. Stavrinidou, D. T. Simon, M. Berggren, S. Fabiano, An evolvable organic electrochemical transistor for neuromorphic applications. *Adv. Sci.* **6**, 1801339 (2019).

62. H. Ling, N. Wang, A. Yang, Y. Liu, J. Song, F. Yan, Dynamically reconfigurable short-term synapse with millivolt stimulus resolution based on organic electrochemical transistors. *Adv. Mater. Technol.* **4**, 1900471 (2019).

63. S. Ginnaram, S. Maikap, Memristive and artificial synapse performance by using TiO_x/Al_2O_3 interface engineering in MoS_2-based metallic filament memory. *J. Phys. Chem. Solid* **151**, 109901 (2021).

64. L. Q. Zhu, C. J. Wan, P. Q. Gao, Y. H. Liu, H. Xiao, J. C. Ye, Q. Wan, Flexible proton-gated oxide synaptic transistors on Si membrane. *ACS Appl. Mater. Interfaces* **8**, 21770–21775 (2016).

65. F. Yu, L. Q. Zhu, W. T. Gao, Y. M. Fu, H. Xiao, J. Tao, J. M. Zhou, Chitosan-based polysaccharide-gated flexible indium tin oxide synaptic transistor with learning abilities. *ACS Appl. Mater. Interfaces* **10**, 16881–16886 (2018).

66. T. Y. Long, L. Q. Zhu, Y. B. Guo, Z. Y. Ren, H. Xiao, Z. Y. Ge, L. Wang, Flexible oxide neuromorphic transistors with synaptic learning functions. *J. Phys. D. Appl. Phys.* **52**, 405101 (2019).

67. S. Park, J. T. Jang, S. J. Choi, D. M. Kim, D. H. Kim, Synaptic behavior of flexible IGZO TFTs with Al_2O_3 gate insulator by low temperature ALD. *Proc. IEEE Conf. Nanotechnol.* **2019**, 517–520 (2019).

68. G. Zhong, M. Zi, C. Ren, Q. Xiao, M. Tang, L. Wei, F. An, S. Xie, J. Wang, X. Zhong, M. Huang, J. Li, Flexible electronic synapse enabled by ferroelectric field effect transistor for robust neuromorphic computing. *Appl. Phys. Lett.* **117**, 092903 (2020).

69. H. Wei, Y. Ni, L. Sun, H. Yu, J. Gong, Y. Du, M. Ma, H. Han, W. Xu, Flexible electro-optical neuromorphic transistors with tunable synaptic plasticity and nociceptive behavior. *Nano Energy* **81**, 105648 (2021).

70. S. H. Jo, T. Chang, I. Ebong, B. B. Bhadviya, P. Mazumder, W. Lu, Nanoscale memristor device as synapse in neuromorphic systems. *Nano Lett.* **10**, 1297–1301 (2010).

71. W. Wu, H. Wu, B. Gao, P. Yao, X. Zhang, X. Peng, S. Yu, H. Qian, A methodology to improve linearity of analog RRAM for neuromorphic computing. *Dig. Tech. Pap. Symp. VLSI Technol.* **2018**, 103–104 (2018).

72. S. Park, A. Sheri, J. Kim, J. Noh, J. Jang, M. Jeon, B. Lee, B. R. Lee, B. H. Lee, H. Hwang, Neuromorphic speech systems using advanced ReRAM-based synapse. *Tech. Dig. Int. Electron Devices Meet. IEDM* **2013**, 625–628 (2013).

73. J. Woo, K. Moon, J. Song, S. Lee, M. Kwak, J. Park, H. Hwang, Improved synaptic behavior under identical pulses using AlO_x/HfO_2 bilayer RRAM array for neuromorphic systems. *IEEE Electron Device Lett.* **37**, 994–997 (2016).

74. D. Kuzum, R. G. D. Jeyasingh, B. Lee, H. P. Wong, Nanoelectronic programmable synapses based on phase change materials for brain-inspired computing. *Nano Lett.* **12**, 2179–2186 (2012).

75. S. Choi, S. H. Tan, Z. Li, Y. Kim, C. Choi, P. Y. Chen, H. Yeon, S. Yu, J. Kim, SiGe epitaxial memory for neuromorphic computing with reproducible high performance based on engineered dislocations. *Nat. Mater.* **17**, 335–340 (2018).

76. M. Jerry, P. Y. Chen, J. Zhang, P. Sharma, K. Ni, S. Yu, S. Datta, Ferroelectric FET Analog synapse for acceleration of deep neural network training, in *Proceedings of the 2017 IEEE International Electron Devices Meeting (IEDM)*, San Francisco, USA, 2 to 6 December 2017.